The Journal of Green Energy and Environmental Engineering

Research Paper

Preparation and High-Temperature Structural Stability of Al_2O_3-Coated SiO_2 Large Hollow Particles

Marisa Champreda[1], Ana Pereira[1], Fredy E. García[2,*]

[1] Laboratorio de Instrumentación Analítica (LIA), Departamento de Química, Facultad Experimental de Ciencias, Universidad del Zulia, Maracaibo, Venezuela
[2] Centro de Estudos Florestais, Instituto Superior de Agronomia, Universidade Técnica de Lisboa, Tapada da Ajuda, 1349-017 Lisboa, Portugal
*Corresponding author: fredygarcia@isa.utl.pt

Abstract. Suppressing the high-temperature sintering of nanoporous thermal insulation materials and enhancing their structural stability is a primary step in extending their service temperature. Al_2O_3-coated SiO_2 large hollow particles (large hollow particle SiO_2@Al_2O_3, diameter ≈130 nm, wall thickness ≈15 nm) were prepared via a hard-template-assisted precipitation method. By synergistically utilizing the anti-sintering property of Al_2O_3 and the low thermal conductivity and low density advantages of SiO_2 hollow structures, the challenge of balancing thermal conductivity and structural thermal stability in traditional thermal insulation materials was addressed. In situ TEM results indicate that when the Al_2O_3 coating content was 3.9% (mass fraction), the particles maintained intact hollow structures after heat treatment at 1200°C for 30 min, with a shrinkage rate <9%; whereas uncoated SiO_2 large hollow particles significantly shrank and ruptured within 2 min. The effective thermal conductivity of this sample was 0.036 $W·m^{-1}·K^{-1}$ at room temperature and only increased to 0.074 $W·m^{-1}·K^{-1}$ at 1100°C, with a density as low as 0.2686 $g·cm^{-3}$, representing a 14% reduction compared to 10 nm solid SiO_2 particles (density 0.3128 $g·cm^{-3}$). Based on molecular dynamics simulations, the high-temperature evolution behavior of these composite particles during heating was systematically revealed, elucidating the mechanism by which the Al_2O_3 shell suppresses the diffusion of liquid-like atoms. This preparation strategy provides experimental and theoretical foundations for the controllable fabrication of lightweight, high-flowability high-temperature thermal insulation powders.

Keywords: *Large hollow particle silica@alumina; Molecular dynamics simulation; High-temperature structural stability; Low thermal conductivity; In situ sintering experiment*

Received on 23 Dec 2025, Accepted on 10 Mar 2026, Published on 24 Apr 2026

1 Introduction

The accelerating advancement of aerospace exploration, high-efficiency energy conversion systems, and extreme-environment industrial technologies has generated an urgent demand for high-performance thermal insulation materials capable of maintaining structural integrity and ultra-low thermal conductivity under sustained high-temperature exposure [1–3]. Critical applications—including reusable launch vehicle thermal protection systems, hot-section components of gas turbines and aviation engines, next-generation nuclear reactor shielding, and energy-saving industrial furnaces—require materials that simultaneously satisfy lightweight, mechanical robustness, chemical inertness, and long-term dimensional stability at temperatures exceeding 1000 °C [4–7]. Traditional high-temperature thermal insulation materials, however, face an entrenched "thermal conductivity–thermal stability" trade-off: strategies that reduce heat transfer frequently compromise structural durability, and vice versa. Porous ceramics such as zirconia and mullite offer moderate insulation but suffer from pore-wall sintering, viscous creep, and progressive densification at elevated temperatures, leading to pore collapse and a sharp rise in thermal conductivity [8, 11]. Refractory fibers, including alumina and aluminosilicate varieties, undergo undesirable crystalline phase transformations above 1000 °C, resulting in embrittlement, pulverization, and irreversible degradation of thermal insulation performance [12]. Nano-porous materials such as SiO_2 aerogels exhibit record-low thermal conductivity at ambient and medium temperatures, yet their nano-scale skeletal structures are highly susceptible to rapid

sintering and densification under thermal loads, causing catastrophic pore-structure collapse [13]. Breaking this performance bottleneck requires innovative material architectures that synergistically integrate low thermal conductivity with intrinsic high-temperature structural stability.

Extensive research efforts have sought to enhance the thermal stability of nano-insulation materials through compositional and microstructural engineering. Increasing the average particle size of nano-building blocks has been shown to reduce surface-area-driven sintering kinetics [14]. Similarly, compounding SiO_2-based matrices with high-melting-point metal oxides—such as ZrO_2, TiO_2, Al_2O_3, and Y_2O_3—can kinetically suppress atomic diffusion and delay structural failure [15–17]. However, these approaches often inadvertently elevate thermal conductivity due to the higher intrinsic thermal conductivities of the stabilizing phases, once again reinforcing the performance trade-off. Microstructural design, particularly the introduction of hollow morphologies, offers a more promising pathway. Hollow nanoparticles encapsulate static gases within closed cavities, minimizing gaseous conduction, while solid–gas interfaces strongly scatter phonons, collectively reducing effective thermal conductivity [18–20]. Further architectural flexibility is achieved through core–shell structuring, where functional shells are deposited onto low-thermal-conductivity cores. Such designs can simultaneously enhance interfacial thermal stability, amplify phonon scattering, and modulate high-temperature radiative heat transfer [21–26]. Among candidate materials, alumina (Al_2O_3) stands out as an ideal shell component due to its high melting point (~2072 °C), excellent chemical inertness, and proven high-temperature structural stability [27]. Silica (SiO_2), conversely, offers intrinsically low thermal conductivity, mature synthetic routes for hollow architectures, and favorable interfacial compatibility with Al_2O_3, making it a preferred core material [28].

While the individual thermal insulation properties of Al_2O_3, SiO_2, and their simple composites have been widely investigated [29–31], the precise regulation of SiO_2@Al_2O_3 core–shell architectures to achieve both ultra-low thermal conductivity and exceptional high-temperature structural stability remains insufficiently explored. Prior studies have seldom addressed the atomic-scale mechanisms governing shell-mediated sintering suppression, nor have they quantitatively optimized shell thickness to avoid unintended side effects such as increased interparticle contact area. Moreover, direct in situ experimental evidence correlating shell coverage with hollow-structure survival under extreme thermal loads is still lacking. To address these gaps, this work proposes a “synergistic thermal enhancement design” based on Al_2O_3-coated SiO_2 large hollow particles (large hollow particle SiO_2@Al_2O_3). The strategy capitalizes on the low thermal conductivity and low density of hollow SiO_2, combined with the anti-sintering capability of an Al_2O_3 shell, to overcome traditional performance limitations. By integrating in situ transmission electron microscopy (TEM) with molecular dynamics (MD) simulations, we elucidate the microscopic mechanism by which the Al_2O_3 shell inhibits the diffusion of surface “liquid-like atoms” during heating. The resulting composite particles exhibit diameters of ~130 nm, wall thicknesses of ~15 nm, densities as low as 0.2686 $g \cdot cm^{-3}$, and room-temperature thermal conductivities of 0.036 $W \cdot m^{-1} \cdot K^{-1}$, while maintaining intact hollow structures after 30 min at 1200 °C. This work thus provides both experimental and theoretical foundations for the rational design of lightweight, high-flowability, high-temperature thermal insulation powders suitable for advanced thermal protection applications.

2. Experiment

2.1 Raw Materials

Reagent-grade styrene (St), polyvinylpyrrolidone (PVP, average molecular weight M≈40000), potassium persulfate (KPS), tetraethyl orthosilicate (TEOS), ammonia solution ($NH_3 \cdot H_2O$, 28%~30% mass fraction), absolute ethanol (EtOH, >99.8%), cetyltrimethylammonium bromide (CTAB), anhydrous aluminum chloride ($AlCl_3$), sodium hydroxide (NaOH), all purchased from Aladdin Reagent (Shanghai) Co., Ltd.; small solid SiO_2 nanoparticles (particle size 10 nm) purchased from Bohua Silicon Nano Technology (Ningbo) Co., Ltd.; deionized water, self-made in the laboratory. All reagents were used directly without further purification.

2.2 Sample Preparation

Al_2O_3-coated SiO_2 large hollow particles (large hollow particle SiO_2@Al_2O_3) composites were prepared using a hard-template-assisted precipitation method. The synthesis of polystyrene template microspheres and the subsequent preparation of SiO_2 large hollow particles followed the literature [32], with optimizations made to

the ratios (specific flow shown in Figure 1): 1) Polystyrene template microsphere synthesis: 1.8 g PVP was ultrasonically dispersed in 90 g of ultrapure water, and 10 g of styrene (PVP/St mass ratio 0.18) was added. Under constant temperature stirring at 70°C and 500 r·min^{-1}, 10 mL of aqueous solution containing 0.18 g KPS was added dropwise to initiate polymerization; the reaction continued for 24 h before cooling to obtain a polystyrene nanosphere dispersion; 2) SiO_2 large hollow particle preparation: 12 g of PS nanosphere dispersion was taken, added to 190 g of ethanol, and magnetically stirred for 15 min. After adding 3 mL of concentrated ammonia, 20 mL of TEOS/ethanol mixture (volume ratio 1:1) was added dropwise in four equal portions, reacting for 24 h. After the reaction, the product was centrifuged, washed twice with ethanol, dried at room temperature, and finally calcined at 500°C for 5 h to remove the polystyrene template, obtaining SiO_2 large hollow particles; 3) Large hollow particle SiO_2@Al_2O_3 preparation: 0.3 g of SiO_2 large hollow particles were dispersed in 70 mL of deionized water, 0.1 g of CTAB was added, magnetically stirred for 0.5 h, then ultrasonically dispersed for 1 h. Subsequently, 0.67 g of $AlCl_3$ was added. After dissolution, 15 mL of 1 mol·L^{-1} NaOH solution was added dropwise in five portions (3 mL each time, at 1 h intervals), with ultrasonic treatment for 15 min after each addition. The resulting suspension was centrifuged (10000 r·min^{-1}, 5 min), washed three times with water, and dried at 100°C to prepare the $Al(OH)_3$-coated precursor. Finally, the precursor was calcined at 1000°C for 2 h to obtain large hollow particle SiO_2@Al_2O_3 with an Al_2O_3 coating layer. Keeping the process parameters unchanged, only adjusting the $AlCl_3$ content, large hollow particle SiO_2@Al_2O_3 with Al/Si ratios of 1% (mass fraction), 5%, and 10% were prepared.

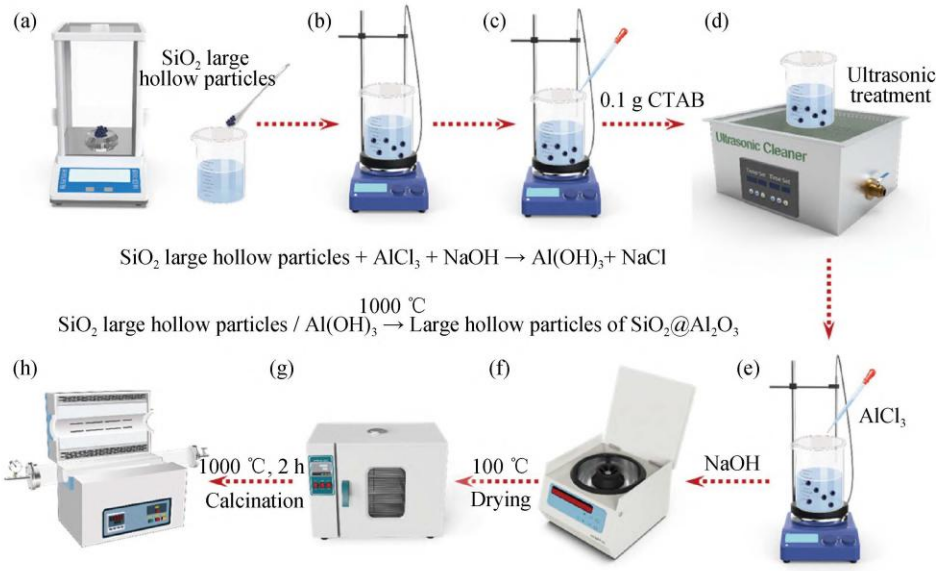

Figure 1 Flow chart for the preparation of large hollow particle SiO2 coated with Al2O3

2.3 Sample Characterization

The density of the samples was determined according to ρ=M/V (where: M is mass; V is volume). All measurements were repeated three times, and the final density value was the average of the three measurements. Transmission electron microscopy (TEM) and energy-dispersive X-ray spectroscopy (EDS) were performed using a Thermo Fisher Talos-F200X instrument to characterize the morphology and microstructure of the materials. Utilizing its high-resolution in situ heating function, the high-temperature structural evolution was observed in real time in a vacuum environment: the sample started heating from 25°C, rose to 500°C within 100 s, and then heated to 1200°C at a rate of 1°C·s^{-1}. Based on the transient plane source method, a Hot Disk TPS2500S thermal constant analyzer (Sweden Hot Disk AB) was used to test the thermal conductivity of the samples, using a 5501F1 polyimide probe for measurement at room temperature. A Netzsch LFA-427 laser flash apparatus was used to test high-temperature thermal conductivity, with a heating rate of 30°C·min^{-1} and a data acquisition frequency up to 2 MHz; three laser flash measurements were performed at each temperature point.

2.4 Metal Oxide-Coated Nanoparticle Model Construction

To investigate the effect of metal oxide coating on the thermal stability of nanoparticles, molecular dynamics processes were calculated using the open-source code LAMMPS (Large-scale Atomic/Molecular Massively Parallel Simulator) [33]. A "melting-annealing" method was used to establish amorphous oxide molecular structures. For the initial crystal structure, a time step of 0.5 fs was set, the initial temperature was 1800 K, and the system was heated to 5000 K under the NVT ensemble with a heating rate of 1×10^{12} K·s^{-1}, holding at 5000 K for 5 ns to allow atoms to detach from the constraints of surrounding atomic interactions and transform into an amorphous state. By hollowing out the obtained amorphous structure into hollow spherical units and further assembling them to construct composite structure models, this work built Al_2O_3-doped solid composite structure models. This work constructed composite structure models of Al_2O_3-doped solid and hollow SiO_2 nanoparticles (Figure 2a). The construction method involved first establishing a SiO_2 nanoparticle molecular model, then coating it with Al_2O_3 nanoparticles. The outer surface area of the particle was marked as Asphere (red), and the inner surface area was marked as Ainner (green). Since the scale of hollow particles (~100 nm) significantly exceeds the molecular simulation scale (~10 nm), and the sintering process is dominated by surface diffusion, nanoparticle sizes of 10 nm and 2 nm were selected for solid SiO_2 and Al_2O_3 as the research objects, respectively. The mass of the SiO_2 hollow particle was defined as msilica, and the mass of coated Al_2O_3 was defined as mAl. Structural evolution during heating was analyzed using a bond-order identification method [34]; for convenience of statistics, the number of "liquid-like atoms" was recorded as N_Liquid, and the total number of atoms was recorded as N_Total [35]. The system was relaxed at 300 K for 1 ns under the NVT ensemble, and then linearly heated to 2000 K within 1 ns. Silica was described using the Tersoff potential function, and alumina nanoparticles were described using the Embedded Atom Method (EAM) potential function. The interaction between silica and alumina was described using the Born-Mayer-Huggins (BMH) potential function and long-range force interactions [36], expressed as:

$$U_{ij}^{BMH} = A_{ij}\exp(\frac{-r_{ij}}{\rho_{ij}}) + \frac{Z_i Z_j e^2}{r_{ij}}\mathrm{erfc}(\frac{r_{ij}}{\beta_{ij}}) \qquad (1)$$

Where: r_{ij} is the distance between ion i and ion j; Z_i and Z_j are the charges of ions i and j, respectively. The first term is the repulsive term; the second term is the Coulomb interaction. The charges for Si, O, and Al are +4, -2, and +3, respectively, with specific parameters listed in Table 1.

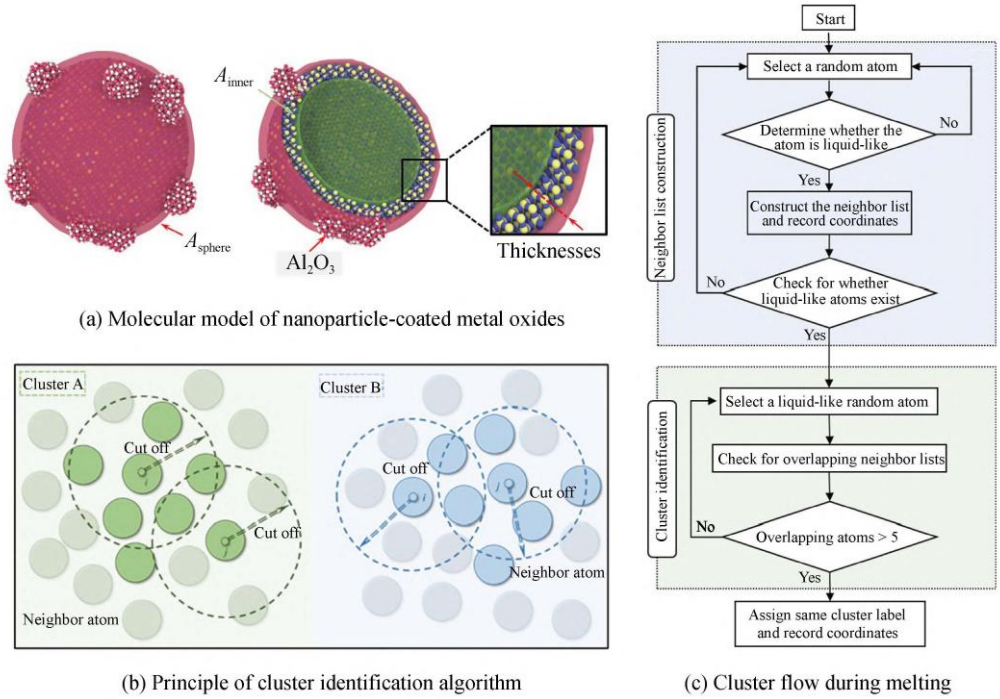

Figure 2 Molecular model of metal oxide coated with nanoparticles and its melting cluster

identification method and evolution process

Table 1 Intermolecular interaction parameters

Interaction	Aij/fJ	βij/pm	ρij/pm
O-O	0.0725	234	29
Si-Al	0.2523	233	29
Al-O	0.2490	234	29
Si-O	0.2962	234	29

Aij is the repulsive-strength prefactor; βij is treated as an interaction-dependent, size-independent parameter; ρ

Ij is the cutoff distance at which the screened Coulomb interaction is truncated.

3. Results and Discussion

To verify the effect of coated metal oxides on the thermal stability of nanoparticles, based on the "bond-order identification" algorithm and according to the change in nearest neighbors of "liquid-like atoms," a "liquid-like atom" neighbor list cluster identification algorithm during heating was proposed. As shown in Figure 2b, for clusters A and B at the current temperature, taking "liquid-like atoms" i and j within cluster A as examples, within the cutoff range of short-range interactions, neighbor lists of "liquid-like atoms" for atoms i and j are established, i.e., counting "liquid-like atoms" of atom i within the cutoff range (1 nm) in cluster A and recording the current coordinates of the atoms. Similarly, statistics are performed for atom j in cluster A, and the corresponding neighbor list is established [37–38]. At the current temperature, for atoms i and j within the same cluster, the neighbor lists overlap, indicating that the two atoms are in the same cluster. For "liquid-like atoms" between different clusters A and B, there is no overlapping neighbor list. The specific calculation method is divided into two main processes: 1) Construction of neighbor lists for "liquid-like atoms"; 2) Cluster identification. The method is as follows: At the current temperature, a random atom is selected, and the bond-order identification algorithm is used to determine whether the atom is a "liquid-like atom." Within a truncation range of 1 nm, a neighbor list for the corresponding atom is established. Similarly, neighbor atom lists are established for all "liquid-like atoms" in the system. By looping through the neighbor lists of each atom, atoms with overlapping neighbor lists are marked as belonging to the same cluster, and atomic coordinates are recorded; the identification process is shown in Figure 2c.

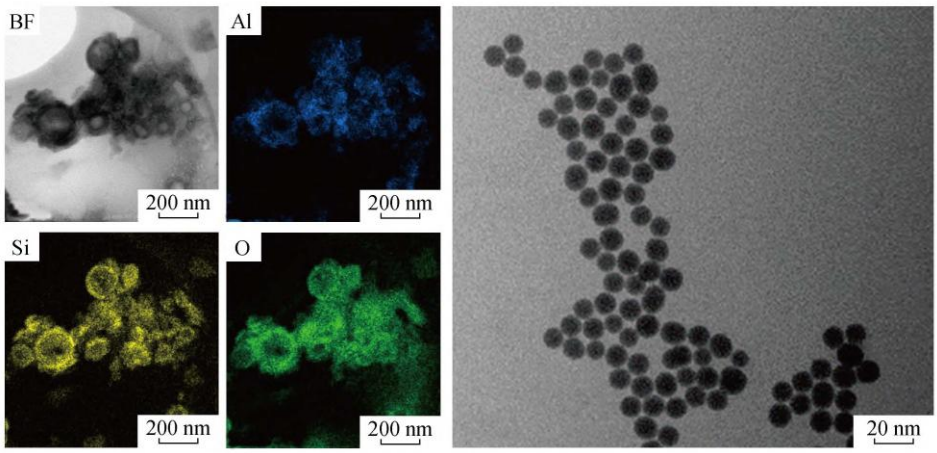

Figure 3 TEM-EDS characterisation of large hollow particles SiO2@Al2O3 and morphology of small solid SiO2 particles

Figure 3 shows TEM-EDS structural verification of large hollow particle SiO_2@Al_2O_3 and TEM images of small solid SiO_2 particles. As shown in Figure 3a, this work successfully prepared a core-shell structure of Al_2O_3-coated SiO_2 large hollow particles (SiO_2@Al_2O_3) with a particle size of approximately 130 nm and a wall thickness of approximately 15 nm. Energy-dispersive X-ray spectroscopy (EDS) elemental analysis confirmed that Al elements were uniformly distributed on the surface of SiO_2 particles, indicating the formation of an effective coating layer. However, when the Al_2O_3 doping amount was high, partial Al_2O_3 formed a covering layer structure between particles, potentially increasing the effective contact area between particles. Figure 3b shows small solid SiO_2 particles with a particle size of about 10 nm and uniform size.

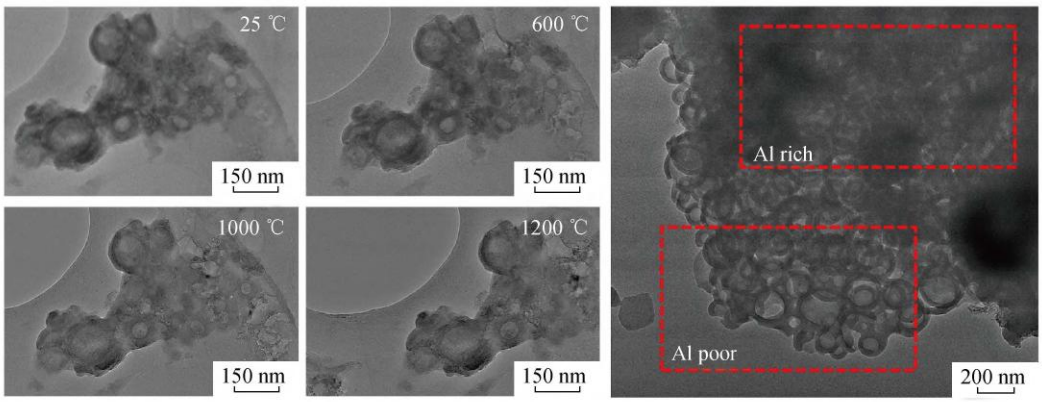

(a) Morphology evolution of high-coated large hollow particles SiO_2@Al_2O_3 by *in-situ* heating

(b) TEM comparison of high/low coating at 1200 ℃ hold 30 min

Figure 4 Morphology evolution of large hollow particles SiO2@Al2O3 after in-situ heating and its coating amount dependence

Figure 4 shows in situ sintered transmission electron microscopy images of large hollow particle SiO_2@Al_2O_3 (held at 1200°C for 30 min). As shown in Figure 4a, Al_2O_3 formed a thicker covering layer on the surface of large hollow particles, increasing the effective contact area between particles. At 1000°C, mass transfer behavior between nanoparticles was observed to a certain extent; at 1200°C, particles shrank significantly, and some hollow structures disappeared, indicating that overly thick coatings promoted sintering and reduced thermal stability. Figure 4b shows a comparison between high-coating (top) and low-coating (bottom) regions after heat treatment at 1200°C for 30 min under the same field of view. The high-coating region showed significant sintering shrinkage, while the low-coating region maintained complete hollow structures, confirming that a small amount of uniformly dispersed Al_2O_3 effectively inhibited sintering.

Figure 5 presents a systematic characterization and comparison of the structural stability at high temperature, density evolution, and thermal conductivity of large hollow particle SiO_2@Al_2O_3 coated with Al_2O_3. As shown in Figure 5a, uncoated SiO_2 large hollow particles experienced obvious shrinkage and rupture after 2 min at 1200°C, with complete structural collapse; whereas large hollow particle SiO_2@Al_2O_3 maintained structural integrity after 30 min under the same conditions, exhibiting excellent anti-sintering performance. As shown in Figure 5b, uncoated SiO_2 large hollow particles: diameter shrinkage rate reached 28% within 2 min, rupture occurred after 5 min; large hollow particle SiO_2@Al_2O_3 (3.9%): diameter shrinkage rate <9% within 30 min, confirming that the Al_2O_3 shell significantly inhibits sintering. As shown in Figure 5c, within the range of 25~1200°C, the density of SiO_2 aerogels and small solid SiO_2 particles increased sharply with temperature: SiO_2 aerogels [39] increased from 0.1864 g·cm^{-3} to 2.0295 g·cm^{-3}, and small solid SiO_2 particles increased from 0.3128 g·cm^{-3} to 2.2634 g·cm^{-3}. In contrast, the density of large hollow particle SiO_2@Al_2O_3 remained basically stable throughout the temperature range, increasing only slightly from 0.2686 g·cm^{-3} at 25°C to 0.2988 g·cm^{-3} after 1200°C, with negligible variation. Further analysis of its thermal conductivity characteristics (Figure 5d) was compared with fiber-reinforced aerogel systems reported in the literature. Although zirconia fiber/zirconia-silica [40], mullite fiber/zirconia-silica [41], quartz fiber/silica-alumina (QF/ASA) [42], and carbon fiber/carbon-alumina composite aerogels [43] maintained low thermal conductivity at high temperatures, their absolute values were generally higher than those of the system in this study. Between 600~1100°C, after incorporating SiO_2 large hollow particles into the

aerogel matrix, the thermal conductivity of the composite increased from 0.055 $W \cdot m^{-1} \cdot K^{-1}$ to 0.067 $W \cdot m^{-1} \cdot K^{-1}$, and that of large hollow particle $SiO_2@Al_2O_3$ increased from 0.059 $W \cdot m^{-1} \cdot K^{-1}$ to 0.074 $W \cdot m^{-1} \cdot K^{-1}$. However, large hollow particle $SiO_2@Al_2O_3$ exhibited a wider high-temperature applicable window and superior thermal stability, offering better prospects for engineering applications.

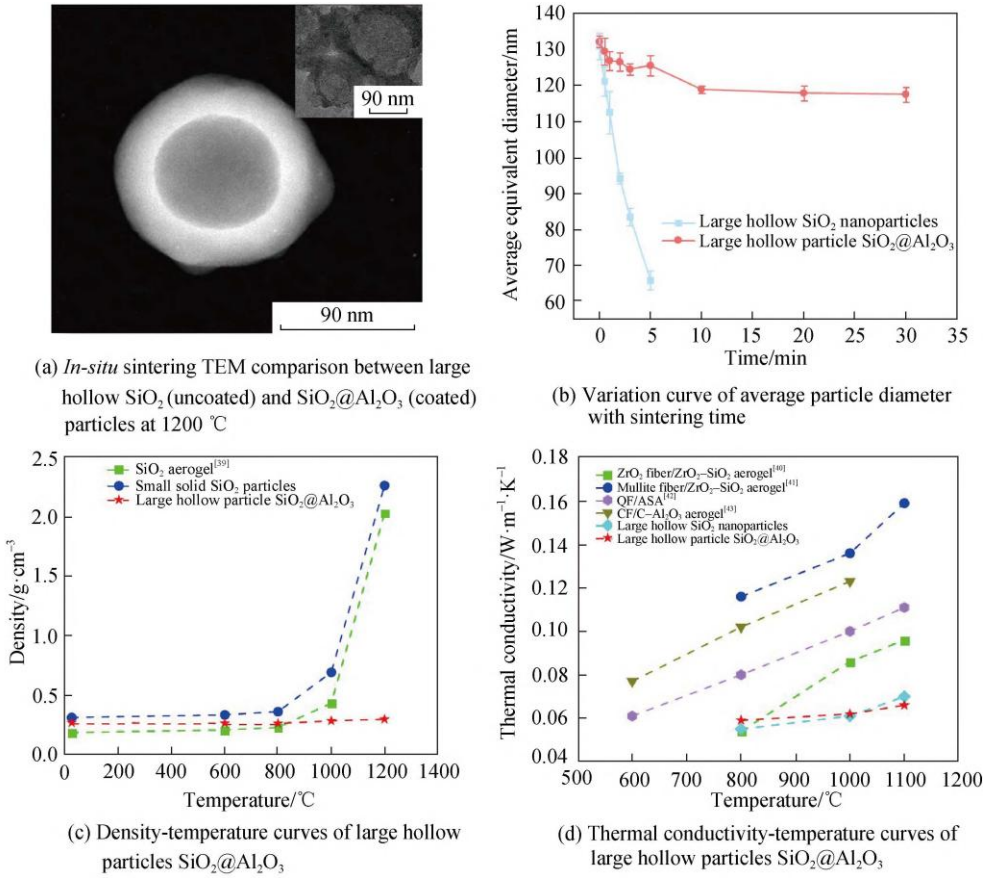

(a) *In-situ* sintering TEM comparison between large hollow SiO_2 (uncoated) and $SiO_2@Al_2O_3$ (coated) particles at 1200 ℃

(b) Variation curve of average particle diameter with sintering time

(c) Density-temperature curves of large hollow particles $SiO_2@Al_2O_3$

(d) Thermal conductivity-temperature curves of large hollow particles $SiO_2@Al_2O_3$

Figure 5 Comparison of sintering behavior of large hollow SiO2 (uncoated) and SiO2@Al2O3 (coated) particles at high temperature: in situ TEM morphology, particle size evolution and structure–thermal stability

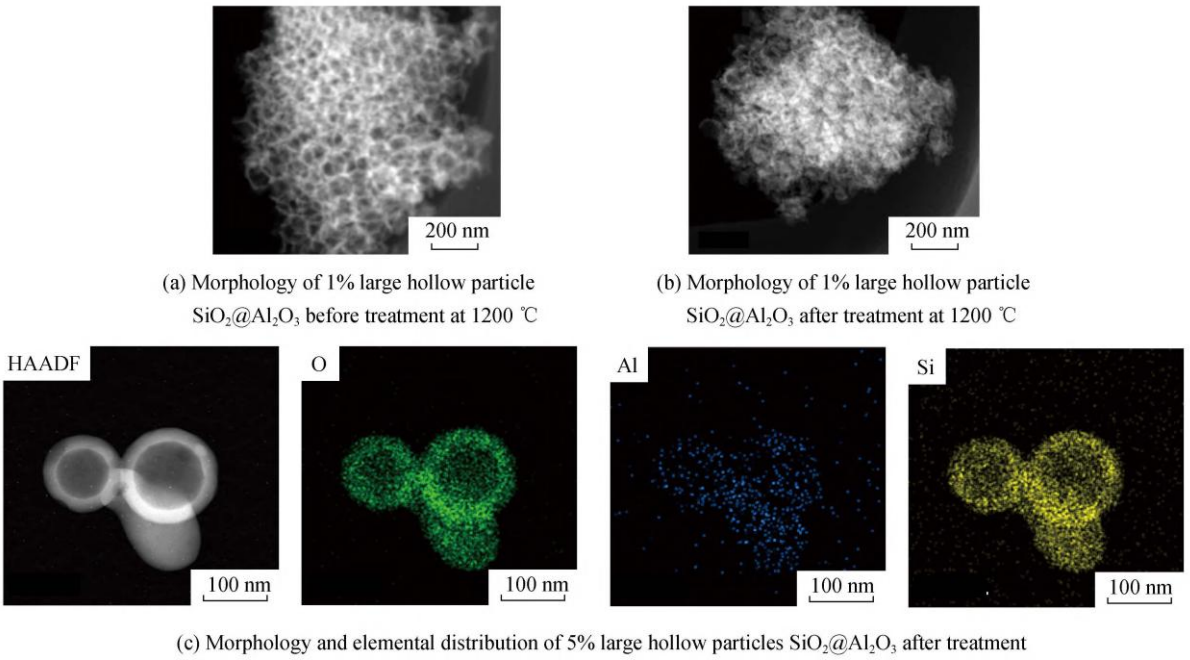

(a) Morphology of 1% large hollow particle $SiO_2@Al_2O_3$ before treatment at 1200 ℃

(b) Morphology of 1% large hollow particle $SiO_2@Al_2O_3$ after treatment at 1200 ℃

(c) Morphology and elemental distribution of 5% large hollow particles $SiO_2@Al_2O_3$ after treatment

Figure 6 Comparison of thermal stability at 1200 ℃of large hollow particles with different contents of SiO2@Al2O3: TEM morphology before and after heat treatment and elemental distribution

Figure 6 shows the TEM morphology and elemental distribution of large hollow particles $SiO_2@Al_2O_3$ with different contents before and after heat treatment at 1200°C. As shown in Figure 6a, the Al_2O_3 coating layer of the 1% sample was discontinuous, and the particles underwent significant shrinkage and local collapse after high-temperature treatment (Figure 6b). In contrast, the 5% sample maintained a complete structural morphology under the same heat treatment conditions without rupture, demonstrating excellent high-temperature resistance (Figure 6c). Elemental analysis of this sample yielded an Al/Si mass ratio of 3.9% (within the allowable error range), further verifying its effective doping and structural stability. Since the density of the 10% sample (ρ=0.3921 g·cm^{-3}) was high, in situ sintering experiments were not conducted. In summary, when the Al/Si doping amount was 3.9%, large hollow particle $SiO_2@Al_2O_3$ exhibited optimal high-temperature structural stability.

Metal oxide coating layers significantly inhibit the sintering process on the surface of nanoparticles at high temperatures. The results of molecular dynamics (MD) simulations are shown in Figure 7. Comparing nanoparticles containing Al_2O_3 coating (3.7%) with uncoated ones, their melting behavior showed significant differences. As temperature increased, the number of surface clusters on the nanoparticles increased first and then decreased, while the cluster size continued to increase. At the same temperature, the number of surface clusters (Figure 7a) of nanoparticles coated with Al_2O_3 was significantly higher than that of uncoated nanoparticles (Figure 7b), confirming that the coating layer effectively inhibited the agglomeration of "liquid-like atoms" and the formation of large-sized clusters. When the temperature reached 1000 K, the cluster numbers of both types of particles decreased significantly; at 1300 K, the cluster number of uncoated particles dropped to 1, indicating that surface fusion was basically complete, while coated particles still maintained 3 clusters at 1500 K (Stage 3). Figure 7c further reveals that in the low-temperature stage (Stage 1), the inhibitory effect of the coating layer was weak; entering the medium-temperature stage (Stage 2), although the cluster size of coated particles continued to grow, its growth rate was significantly limited, indicating that the metal oxide coating layer effectively prevented the rapid fusion of "liquid-like atoms." In contrast, uncoated particles (Figure 7d) underwent rapid cluster fusion and overall particle melting at approximately 1000 K (Stage 3). Therefore, the metal oxide coating layer significantly prolonged the transition process of nanoparticles from stable cluster growth (Stage 2) to rapid complete melting (Stage 3) by inhibiting cluster fusion.

The melting process of nanoparticles usually includes three stages: surface diffusion, transition point, and volume diffusion [44]. Metal oxide-coated nanoparticles also follow this rule. Figure 8 shows the three stages of

sintering evolution for large hollow particles coated with metal oxides. As shown in Figure 8, with increasing temperature, "liquid-like atom" clusters gradually formed on the particle surface. When the temperature further increased, these clusters connected and fused with each other, promoting the rapid melting of the coated metal oxides. In this process, the doped metal oxides melted rapidly under the coating of "liquid-like atom" clusters, but the presence of multiple metal oxides hindered the diffusion and fusion of "liquid-like atom" clusters, thereby prolonging the transition process from surface diffusion to volume diffusion. When "liquid-like atom" clusters rapidly condensed to form larger clusters near the transition point, regions not covered by metal oxides had already melted first, while regions covered by multiple metal oxides significantly hindered cluster diffusion. As the temperature continued to rise, the diffusion mechanism of "liquid-like atom" clusters shifted from surface diffusion to volume diffusion. At this point, the silica matrix with a relatively low melting point melted rapidly, leaving only a small amount of unmelted metal oxide particles.

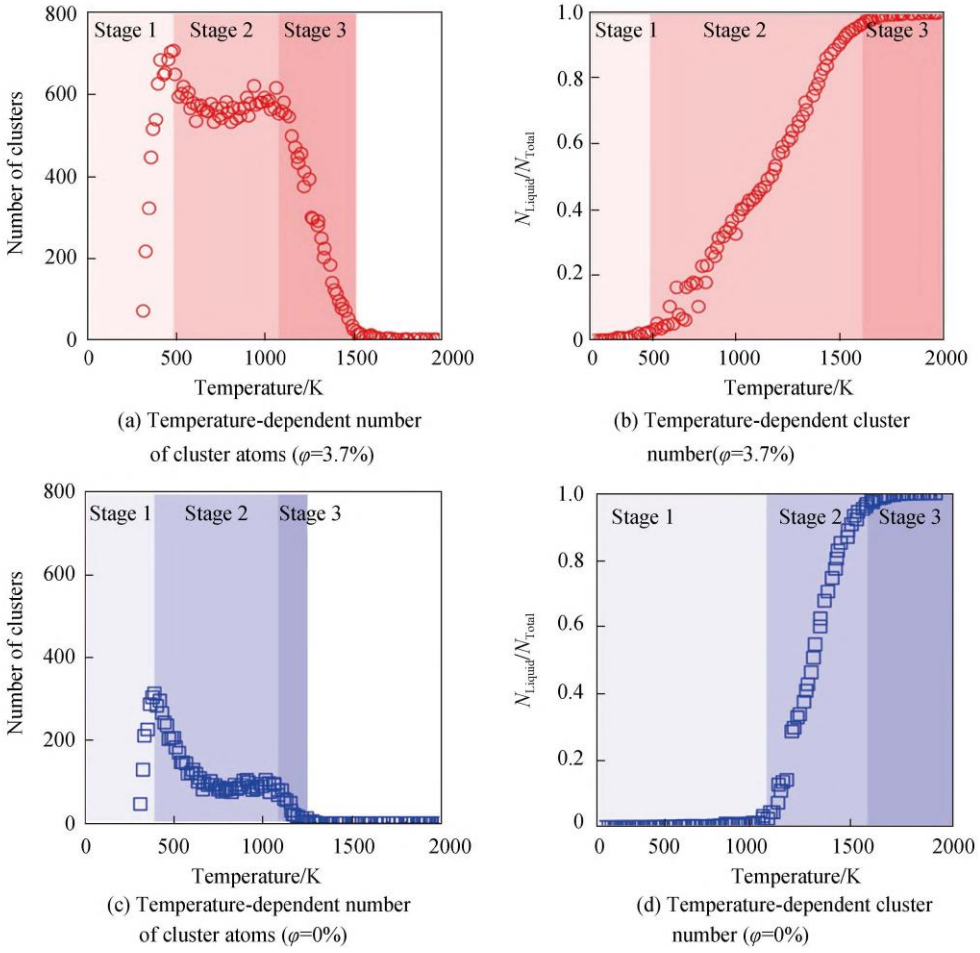

Figure 7 Variations in number of atoms of melting clusters, and number of clusters on surface of large hollow particles coated with metal oxides during melting process

This study establishes a clear structure–property relationship for Al_2O_3-coated SiO_2 large hollow particles, demonstrating that a thin, discontinuous Al_2O_3 shell (~3.9 wt%) is the key to simultaneously achieving ultra-low thermal conductivity and exceptional high-temperature structural stability. In situ TEM sintering experiments reveal a stark mechanistic contrast: uncoated SiO_2 hollow particles undergo rapid shrinkage and rupture within 2 minutes at 1200 °C, whereas the 3.9% Al_2O_3-coated counterparts retain intact hollow morphologies for 30 minutes, with a radial shrinkage rate of less than 9%. This dramatic improvement stems from the Al_2O_3 shell acting as a diffusion barrier that suppresses surface atomic mobility and prevents the coalescence of neighboring particles. Importantly, the study identifies a critical “over-coating” threshold: when the Al/Si mass ratio reaches 10%, excessive Al_2O_3 forms a continuous covering layer that bridges adjacent particles, increasing effective contact area and accelerating sintering rather than preventing it. This finding resolves a long-standing ambiguity

in ceramic coating design—namely, that anti-sintering efficacy is not monotonic with coating thickness, but instead exhibits an optimum regime where interfacial protection outweighs geometric drawbacks. From a thermal transport perspective, the large hollow architecture capitalizes on confined air domains and enhanced phonon scattering at solid–gas interfaces to offset the inherently higher thermal conductivity of Al_2O_3. Consequently, the optimized composite achieves a room-temperature thermal conductivity of 0.036 $W \cdot m^{-1} \cdot K^{-1}$ and maintains 0.074 $W \cdot m^{-1} \cdot K^{-1}$ even at 1100 °C, outperforming conventional fiber-reinforced aerogels and dense solid SiO_2 particles. The density advantage is equally pronounced: at 0.2686 $g \cdot cm^{-3}$, the composite is ~14% lighter than 10 nm solid SiO_2, underscoring its suitability for weight-sensitive aerospace and mobile energy systems.

Molecular dynamics simulations complement the experimental observations by elucidating the atomic-scale origin of the shell's anti-sintering behavior. By introducing a "liquid-like atom" cluster identification algorithm, the study tracks the evolution of surface diffusion processes across temperatures ranging from 300 K to 2000 K. The results show that Al_2O_3 doping increases the number of discrete surface clusters while restricting their lateral growth, effectively delaying the transition from Stage 2 (surface diffusion) to Stage 3 (volume diffusion and complete melting). Specifically, uncoated SiO_2 particles experience full surface fusion at ~1000 K, whereas coated particles retain multiple independent clusters up to 1500 K, confirming that the shell acts as a kinetic bottleneck for atomic rearrangement. The BMH potential-based interaction model further reveals that the Al_2O_3 shell modifies the local coordination environment and raises the energetic barrier for Si–O bond reorganization, thereby stabilizing the amorphous silica framework. These insights extend beyond thermal insulation, offering a generalized design principle for suppressing sintering in other high-temperature nanomaterials, such as catalysts, sensors, and functional coatings. While the current study focuses on laboratory-scale synthesis, the hard-template precipitation route is scalable and compatible with industrial slurry processing, spray drying, and additive manufacturing. Future work should explore multi-element shell compositions (e.g., Al_2O_3–ZrO_2 or Al_2O_3–Y_2O_3) to further elevate the service temperature ceiling and tailor radiative heat transfer properties. Additionally, integrating these particles into 3D-printed scaffolds or electrospun fibrous mats could unlock new opportunities in multifunctional thermal protection systems. Overall, this work provides a robust materials platform that reconciles the historically conflicting demands of low thermal conductivity, low density, and high-temperature structural stability, marking a significant step forward in extreme-environment insulation technology.

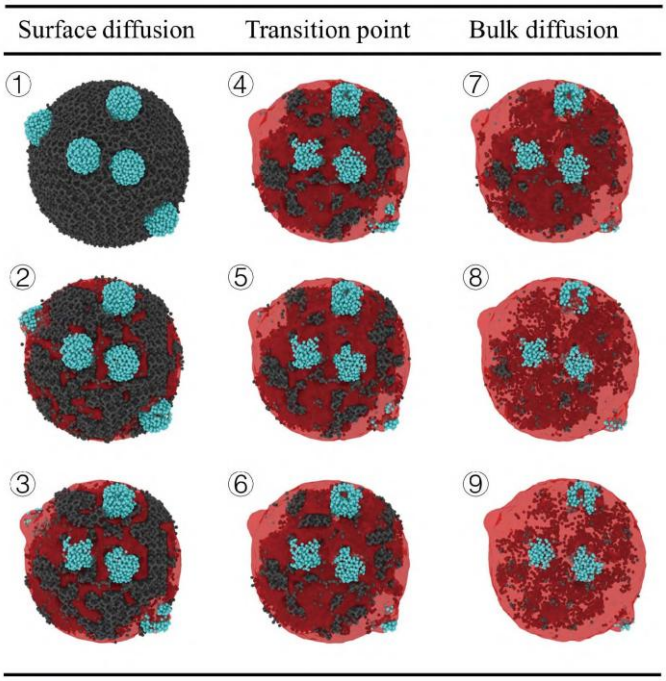

Figure 8 Three stages of sintering evolution of metal oxide coated with large hollow particles: surface diffusion– transition point–bulk diffusion

4. Conclusion

Focusing on breaking through the bottleneck where high-temperature structural thermal stability, low thermal conductivity, and low density are difficult to balance in high-temperature insulation materials, this work designed and prepared large hollow particle SiO_2@Al_2O_3. Through in situ sintering experiments and molecular dynamics simulations, the following main conclusions were obtained:

Al_2O_3 uniformly coated SiO_2 large hollow particles (particle size ≈130 nm, wall thickness ≈15 nm) were prepared using a hard-template-assisted precipitation method. When Al/Si = 3.9% (mass fraction), large hollow particle SiO_2@Al_2O_3 exhibited excellent high-temperature thermal stability. Excessive doping levels formed a continuous Al_2O_3 covering layer, increasing the contact area between particles and promoting surface mass transfer, which led to a decrease in thermal stability.

The large hollow particle SiO_2@Al_2O_3 with a doping amount of 3.9% showed a density increase from 0.2686 $g·cm^{-3}$ to only 0.2988 $g·cm^{-3}$ in the range of 25~1200°C; the effective thermal conductivity increased from 0.036 $W·m^{-1}·K^{-1}$ to 0.074 $W·m^{-1}·K^{-1}$. In situ heating TEM confirmed that this sample maintained an intact hollow structure after holding at 1200°C for 30 min, with a radial shrinkage rate <9%, and its anti-sintering performance was significantly better than that of undoped SiO_2 large hollow particles (rapid sintering failure). Its room-temperature thermal conductivity (0.036 $W·m^{-1}·K^{-1}$) was comparable to that of the undoped system (0.035 $W·m^{-1}·K^{-1}$), and the density was 14% lower than that of traditional 10 nm solid SiO_2 particles (0.3128 $g·cm^{-3}$), indicating that Al_2O_3 doping significantly improved high-temperature structural thermal stability while maintaining ultra-low thermal conductivity and low density, overcoming the trade-off dilemma between high-temperature structural thermal stability and insulation performance in traditional modification.

Based on molecular dynamics simulations, a nanoparticle model doped with metal oxides on the surface was constructed to study its structural evolution during heating. Based on the "liquid-like atom" cluster identification algorithm, the dynamic changes of surface clusters were accurately tracked, and the doped metal oxides could effectively inhibit the surface diffusion of "liquid-like atoms."

Large hollow particle SiO_2@Al_2O_3 possesses characteristics such as low density, high flowability, and high-temperature structural stability, allowing it to be combined with technologies like 3D printing and electrospinning. This provides a new pathway for designing thermal insulation materials that meet diverse thermal protection needs, offering significant application potential in extreme environment thermal protection, additive manufacturing of lightweight complex structures, and preparation of high-performance flexible thermal insulation fiber membranes.

References

[1] ZHANG Q, HUANG H Y, LEI C S, et al. Review of lightweight, high-temperature thermal insulation materials for aerospace. Materials, 2025, 18(10): 2383.
[2] JIANG P X, JIN H G. Strategic research on frontier interdisciplinary fields in energy conversion and utilization for "Dual Carbon" goals. Chin Sci Bull, 2024, 69(34): 5007–5015.
[3] JIAN Y, JIANG Y G, FENG J Z, et al. Preparation, properties, and applications of waterproof high-temperature insulation materials. J Chin Ceram Soc, 2025, 53(3): 718–732.
[4] SUN F H, YANG J, ZHENG M B, et al. Research progress on thermal protection functional fibers and smart textiles. Chin Sci Bull, 2025, 70(17): 2718–2732.
[5] CHEN X Y, CHEN Y L, PENG X B, et al. Research progress on preparation, structure, and application of thermal insulation materials. CIESC J, 2025: 1–24.
[6] LI J N, FENG Z H, ZHANG D H, et al. Research progress on reusable thermal protection materials. Aerosp Mater Technol, 2024, 54(2): 1–10.
[7] MEN J, FENG J Z, JIANG Y G, et al. Research progress on sol-gel synthesis process and related structure of carbon aerogels. J Chin Ceram Soc, 2024, 52(8): 2709–2721.
[8] GUO J R, FU S B, DENG Y P, et al. Hypocrystalline ceramic aerogels for thermal insulation at extreme conditions. Nature, 2022, 606(7916): 909–916.
[9] ZHAO K, YE F, CHENG L F, et al. An overview of ultra-high temperature ceramic for thermal insulation:

Structure and composition design with thermal conductivity regulation. J Eur Ceram Soc, 2023, 43(16): 7241–7262.
[10] LU Q, HU L F, LUO X G, et al. Research progress on ceramic composites and thermal structures for hypersonic vehicles. J Chin Ceram Soc, 2013, 41(2): 251–260.
[11] ZHAO H F, SUN W C, ZHOU L, et al. Preparation and thermal conductivity of fiber-reinforced ZrO_2 foam ceramics. J Funct Mater, 2023, 54(12): 12012–12017.
[12] ZOU T, LI Z L, WANG D, et al. Calcination kinetics of α-Al_2O_3 based on multi-scanning rate method. Min Metall Eng, 2024, 44(2): 106–111.
[13] XU M J, LIU Q, LI L, et al. Preparation and thermal insulation properties of low-temperature carbonization and high-temperature service carbon aerogel composites. Acta Mater Compos Sin, 2025, 42: 1–9.
[14] TALYZIN I V, SAMSONOV M V, SAMSONOV V M, et al. Size dependence of the melting point of silicon nanoparticles: Molecular dynamics and thermodynamic simulation. Semiconductors, 2019, 53(7): 947–953.
[15] WANG X, HUANG J, ZHENG Z R. Preparation of TiO_2/SiO_2 aerogel thermal insulation coating tent material. China Dye Finish, 2020, 46(1): 52–55.
[16] ZHU W X, WANG H, JI H M, et al. Preparation and high-temperature thermal insulation properties of lightweight and high-strength silica oxycarbide aerogels. J Chin Ceram Soc, 2024, 52(9): 2773–2779.
[17] NI Y Y, ZHU J Y, GAO Y, et al. Preparation of silica aerogels based on ternary phase transition control. J Chin Ceram Soc, 2024, 52(8): 2685–2694.
[18] LIU H, TIAN Y, MOFID S A, et al. Numerical modeling of effective thermal conductivity of hollow silica nanosphere packings. Int J Heat Mass Transf, 2022, 182: 122032.
[19] DU H, LIU S L, ZHANG Y Y, et al. Hollow structure construction of silicon-based anode materials and lithium storage performance. Chin Sci Bull, 2024, 69(16): 2145–2156.
[20] XIAO W, JIANG Q L, YANG X Y, et al. Template synthesis of iron phosphide hollow nanorods and their electrochemical properties. J Chin Ceram Soc, 2023, 51(7): 1724–1732.
[21] LI T, ZHOU W Y, CAO D, et al. Research progress on core-shell particle/polymer composite dielectric materials. Mod Plast Process Appl, 2021, 33(1): 60–63.
[22] LI B, XIAO Y S, LIU Z T, et al. High-performance Ni/SiO_2@La_2O_3 core-shell catalyst for dry reforming of methane. Chin Sci Bull, 2025, 70(13): 1954–1965.
[23] ZHOU X, CHEN P, LIU Y, et al. Preparation and lithium storage performance of ZIF-derived hollow NiS_2/CoS_2@HNC. Chin Sci Bull, 2024, 69(3): 464–472.
[24] ZHANG Y F, QIN Z F, LU J J, et al. Preparation and performance of core-shell structure C@Ni methanation catalyst. Nat Gas Chem Ind, 2018, 43(6): 11–16.
[25] ZHAO Y, ZHOU H, LI Z, et al. Research progress on preparation and flame retardancy strategies of core-shell structure flame retardants. New Chem Mater, 2023, 51(8): 71–78.
[26] ZHAN H Q, WU C Q, SONG Y H, et al. Enhancement mechanism of glaze surface visible light reflection based on amorphous photonic crystal structure. J Chin Silic Soc, 2020, 48: 894–902.
[27] PENG Q Q, FANG H, CHENG Z Y, et al. Research progress on application of fine alumina. China Resour Compr Util, 2023, 41(7): 118–121.
[28] ZHANG W L, XIAO D H, DING D Y. A first-principles investigation of interfacial properties and electronic structure of SiO_2/Al interface. Comput Mater Sci, 2021, 188: 110228.
[29] REN H, TONG T B, LIU M, et al. Temperature resistance of alumina aerogels. Refractories, 2024, 58(4): 297–301.
[30] AI S F, WANG S, YANG G X, et al. Thermal insulation properties of silica aerogel composites with different densities under low-temperature vacuum environment. J Beijing Univ Chem Technol (Nat Sci Ed), 2023, 50(1): 65–71.
[31] ZHANG Y, GAO X D, YAO J Q, et al. Research progress on preparation technology of SiO_2-Al_2O_3 aerogels and fiber-reinforced composites. Mater Rep, 2022, 36(23): 57–65.
[32] GAO T, JELLE B P, SANDBERG L I C, et al. Monodisperse hollow silica nanospheres for nano insulation materials: Synthesis, characterization, and life cycle assessment. ACS Appl Mater Interfaces, 2013, 5(3): 761–767.
[33] THOMPSON A P, AKTULGA H M, BERGER R, et al. LAMMPS—A flexible simulation tool for particle-based materials modeling at the atomic, meso, and continuum scales. Comput Phys Commun, 2022, 271: 108171.
[34] LECHNER W, DELLAGO C. Accurate determination of crystal structures based on averaged local bond order parameters. J Chem Phys, 2008, 129(11): 114707.
[35] CHANG C, ZHANG H P, ZHAO R, et al. Liquid-like atoms in dense-packed solid glasses. Nat Mater, 2022,

21(11): 1240–1245.

[36] MA F R, WEI B, MAIERHABA A, et al. Analysis of the influence of silica-alumina ratio on the microstructure of CaO-SiO_2-Al_2O_3 melts. Clean Coal Technol, 2021, 27(4): 189–194.

[37] SHIRE T, HANLEY K J, STRATFORD K. DEM simulations of polydisperse media: Efficient contact detection applied to investigate the quasi-static limit. Comput Part Mech, 2021, 8(4): 653–663.

[38] MONTI J M, CLEMMER J T, SRIVASTAVA I, et al. Large-scale frictionless jamming with power-law particle size distributions. Phys Rev E, 2022, 106(3): 034901.

[39] CAI H F, JIANG Y G, FENG J, et al. Nanostructure evolution of silica aerogels under rapid heating from 600 ℃ to 1300 ℃ via in situ TEM observation. Ceram Int, 2020, 46(8): 12489–12498.

[40] HE J, ZHAO H Y, LI X L, et al. Large-scale and ultra-low thermal conductivity of ZrO_2 fibrofelt/ZrO_2-SiO_2 aerogels composites for thermal insulation. Ceram Int, 2018, 44(8): 8742–8748.

[41] ZHANG R B, HOU X B, YE C S, et al. Enhanced mechanical and thermal properties of anisotropic fibrous porous mullite-zirconian composites produced using Sol-gel impregnation. J Alloys Compd, 2017, 699: 511–516.

[42] YU H J, TONG Z W, ZHANG B J, et al. Thermal radiation shielded, high strength, fire resistant fiber/nanorod/aerogel composites fabricated by in situ growth of TiO_2 nanorods for thermal insulation. Chem Eng J, 2021, 418: 129342.

[43] ZHONG Y, ZHANG J J, WU X D, et al. Carbon-fiber felt reinforced carbon/alumina aerogel composite fabricated with high strength and low thermal conductivity. J Sol Gel Sci Technol, 2017, 84(1): 129–134.

[44] YANG M Y, TANG G H, SHENG Q, et al. Atomic-level sintering mechanism of silica aerogels at high temperatures: Structure evolution and solid thermal conductivity. Int J Heat Mass Transf, 2022, 199: 123456.